






# A Feasibility Study on Wide Swath Observation by Spaceborne Precipitation Radar

Kosuke Yamamoto , Takuji Kubota , *Member, IEEE*, Nobuhiro Takahashi , Kaya Kanemaru , Takeshi Masaki , and Kinji Furukawa

**Abstract**—A feasibility study on wide swath observation assuming future spaceborne precipitation radar was demonstrated using data obtained from a wide swath observation experiment conducted in September 2017 by using the dual-frequency precipitation radar onboard the global precipitation measurement core observatory. In this experiment, scan angles of the Ku-band precipitation radar (KuPR) and Ka-band precipitation radar (KaPR) were experimentally changed to observe from nadir to about  $+34^\circ$ . While the result showed that the precipitation echo could be obtained at wider scan angles, the occurrence of sidelobe and grating lobe clutters not seen in a normal scan were simultaneously observed. The mainlobe clutter height of KuPR increased linearly along the incident angle, and 0.5 mm/h precipitation may be masked up to 4 km over land at the angle of  $+34^\circ$ . Besides, the grating lobe clutter clearly occurred in KuPR when the ground surface of the grating lobe direction was land or sea ice. The maximum scan angle without the grating lobe contamination was  $+23.43^\circ$ , approximately corresponding to 355 km swath width with the orbit altitude of 407 km. For KaPR, the grating lobe contamination was not significant and the mainlobe clutter height peaked at the scan angle of around  $26^\circ$ , and then tended to decrease at larger scan angles. Therefore, precipitation at the lower altitude may have a chance to be detected even at larger scan angles, while weaker surface echoes at larger scan angles may need new techniques to estimate precipitation for the KaPR.

**Index Terms**—Meteorological radar, radar clutter, spaceborne radar.

## I. INTRODUCTION

**F**OLLOWING the successful observation by the precipitation radar (PR) onboard the tropical rainfall measuring mission (TRMM) [1], [2], the dual-frequency precipitation radar (DPR) onboard the global precipitation measurement (GPM)

core observatory was developed as the first space-based DPR consisting of Ku-band precipitation radar (KuPR) and Ka-band precipitation radar (KaPR) [3]–[8]. The combined use of the DPR and the GPM microwave imager (GMI) onboard the GPM core observatory has improved the technique of precipitation estimation and plays an important role as a calibrator for global precipitation datasets [9]–[12]. Despite these significant contributions, spaceborne PRs are still expected to be improved for some functions. One major requirement is extension of swath width. The spaceborne radars such as PR and DPR are phased array radars that scan electrically and rapidly in the cross-track direction. The KuPR swath width is approximately 245 km, which corresponds to  $\pm 17^\circ$  electrical beam scanning when the GPM core observatory flies at an altitude of 407 km. However, the current swath width is not always satisfied for disaster monitoring that is induced by heavy precipitation. The Japan Meteorological Agency (JMA) began DPR assimilation in the operational mesoscale numerical weather prediction system on March 24, 2016 [13]. In operational uses of the spaceborne radar data as by the JMA, wide swath observations are highly required to increase observation frequencies.

Using the data obtained from the TRMM PR end-of-mission experiment [14], the feasibility of wide swath observation was examined by Takahashi [15], assuming a maximum scan angle of  $32.5^\circ$  for KuPR. Takahashi [15] statistically assessed the mainlobe clutter height that masks the precipitation echo near the earth's surface and stated the possibility of heavy precipitation retrieval in terms of the received echo power even when the scan angle is large. However, examination of the maximum radar scan angle in consideration of the sidelobe and/or grating lobe clutter occurrences remain as an issue. Besides, further investigations not only from received echo power but also from actual precipitation intensity's point of view need to be strengthened. Considering the situation that the dual-frequency observation is now utilized in techniques for more accurate precipitation estimates (e.g., [16] and [17]), these discussions should be extended to multiple frequencies when assuming the future spaceborne PR. To assess the possibility of wide swath observation by multiple frequencies, a wide swath observation experiment of the DPR was conducted on September 26 and 27, 2017. Wider swath observation data by DPR can provide new viewpoints beyond the single-frequency observations by the TRMM PR.

The purpose of this article is to reveal the feasibility of wide swath observation assuming future spaceborne PR in terms of the

Manuscript received March 30, 2020; accepted May 16, 2020. Date of publication June 1, 2020; date of current version June 18, 2020. (*Corresponding author: Kosuke Yamamoto.*)

Kosuke Yamamoto and Takuji Kubota are with the Earth Observation Research Center, Japan Aerospace Exploration Agency, Tsukuba 305-8505, Japan (e-mail: yamamoto.kosuke@jaxa.jp; kubota.takuji@jaxa.jp).

Nobuhiro Takahashi is with the Institute for Space-Earth Environmental Research, Nagoya University, Nagoya 464-8601, Japan (e-mail: ntaka@nagoya-u.jp).

Kaya Kanemaru is with the Applied Electromagnetic Research Institute, National Institute of Information and Communications Technology, Tokyo 184-8795, Japan (e-mail: kanemaru@nict.go.jp).

Takeshi Masaki is with the Earth Environment Data Analysis and Research Group, Remote Sensing Technology Center of Japan, Tsukuba 305-8505, Japan (e-mail: masaki\_takeshi@restec.or.jp).

Kinji Furukawa is with the Satellite Applications and Operations Center, Japan Aerospace Exploration Agency, Tsukuba 305-8505, Japan (e-mail: furukawa.kinji@jaxa.jp).

Digital Object Identifier 10.1109/JSTARS.2020.2998724

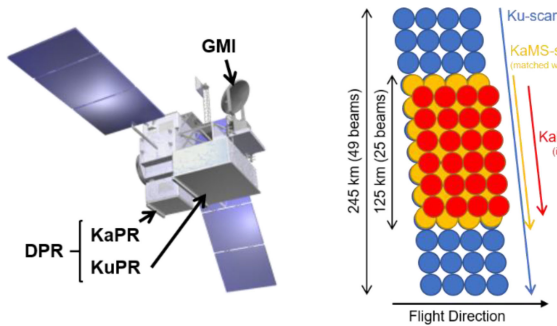


Fig. 1. Schematic of the GPM core satellite and antenna scanning geometry in KuPR and KaPR before May 21, 2018.

clutter contamination and precipitation detection. In this study, we assume the specification of the DPR as the baseline for future spaceborne PR to make the most of the data obtained from the DPR wide swath observation experiment. An overview of the GPM DPR and details of the wide swath observation experiment are presented in the next section. Section III describes the method of radar clutter analysis and the characteristics of clutters that occurred during the experiment, and Section IV investigates the capability of detecting precipitation by wide swath observation. Section V discusses the limitations and applicability of wide swath operation for future spaceborne precipitation radars, and then summarizes this article.

## II. DATA

### A. GPM DPR Instrument Overview

The DPR is the first space-based DPR, jointly developed by the Japan Aerospace Exploration Agency (JAXA) and the National Institute of Information and Communications Technology [5], [8]. Fig. 1 illustrates the specifications of the GPM core observatory. The GPM Core Observatory flies at an altitude of about 407 km, carrying the GMI and the DPR. The DPR is phased array radar consisting of the KuPR and the KaPR, and scans with three different modes: Ku, KaMS (matched scan), and KaHS (high-sensitivity scan). Ku scans with a width of about 245 km by using 49 beams, and KaMS simultaneously scans with the inner 25 beams of Ku. KaHS is an interlaced scan shifted half a scan angle within the inner swath which consists of 24 beams. This scan pattern was a baseline for the wide swath observation experiment conducted in 2017 as described in the next section, whereas the KaPR scan pattern was changed to full swath ( $\pm 17^\circ$ ) observation on May 21, 2018. The horizontal resolution on the ground is about 5.2 km for all scan modes, and the range resolution is 250 m for both Ku and KaMS scans, and 500 m for KaHS scan.

### B. Wide Swath Observation Experiment

Fig. 2(a) illustrates the number of KuPR normal observations ( $\pm 17^\circ$  scan) in  $0.1^\circ$  lat/lon grid for 16 orbits. The total area covered by the satellite footprint is very sparse and observed once or twice at most per grid. To increase the observation frequency, simulation assuming the doubled swath ( $\pm 34^\circ$  scan)

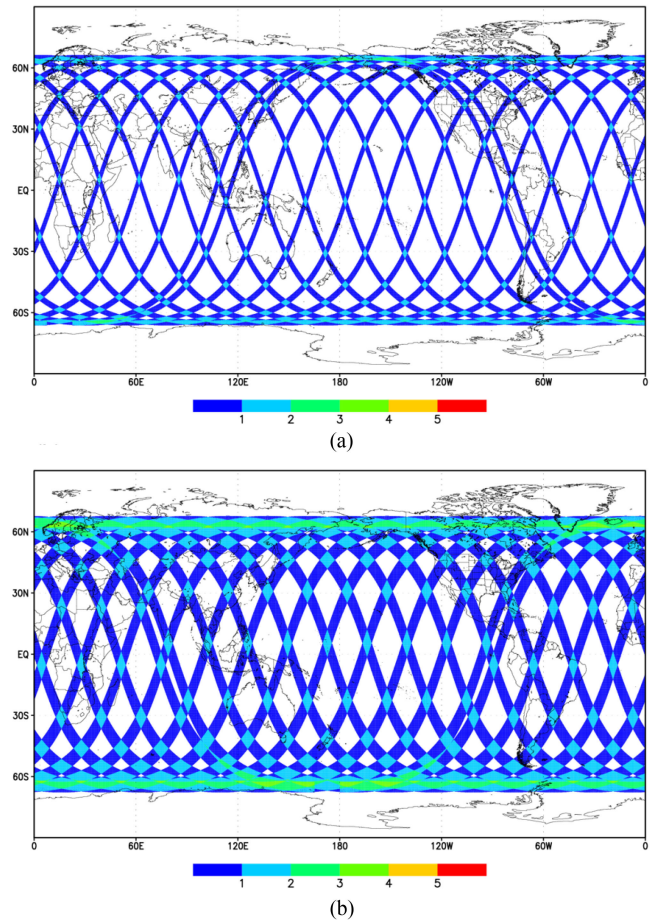


Fig. 2. Number of DPR observations in  $0.1^\circ$  lat/lon grid for 16 orbits. (a) Based on data during normal observation ( $\pm 17^\circ$  scan). (b) Based on the simulated result assuming the  $\pm 34^\circ$  scan around nadir.

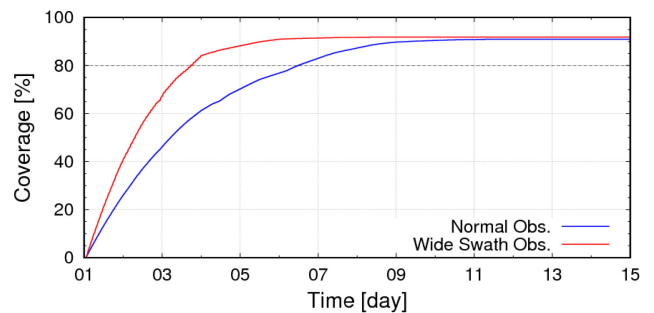


Fig. 3. Time series of the percentage of observed area by DPR to the surface area of the earth. The blue line denotes the result from normal observation; the red line is based on the simulation result assuming the  $\pm 34^\circ$  scan around nadir.

is conducted. Note that the  $\pm 34^\circ$  scan is roughly equivalent to 550 km, whereas the operational swath width of the KuPR is about 245 km in the normal observation. Fig. 2(b) shows the same plot as in Fig. 2(a) for the simulation result, indicating that the doubled swath enables us to access more frequent observation, especially in high latitude areas (3–4 times in 16 orbits). Fig. 3 shows the change over time in the ratio of observed area to the earth's surface, in the case of Fig. 2(a) and (b). In the

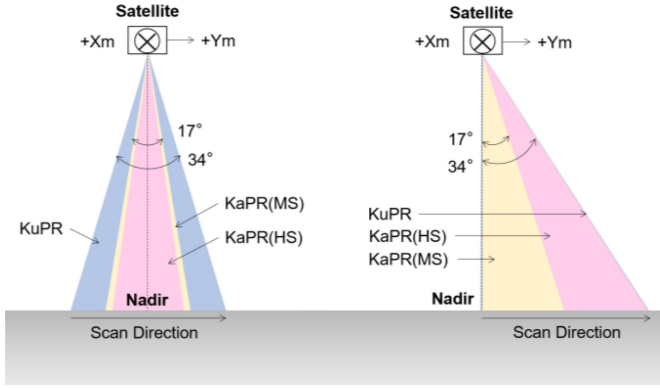


Fig. 4. Conceptual diagram of the DPR scan patterns during normal observation (left) and wider swath experimental observation in September 2017 (right).

simulation, the scanning radar is mounted on the same orbit of the GPM Core Observatory whose maximum coverage of the earth surface is approximately 92% and the scanning speed for  $\pm 34^\circ$  is set the same as that for the KuPR's  $\pm 17^\circ$  scan in the normal observation. The results show that the time required for the observation area to reach 80% of the earth's surface is about three days earlier than in the normal observation ( $\pm 17^\circ$ ), suggesting that the experiment setting assuming the  $\pm 34^\circ$  scan is sufficiently effective for increasing the observation frequency.

In order to investigate the possibility of wide swath observation by multiple frequencies based on the abovementioned discussions, a wide swath observation experiment using the DPR was conducted on September 26 and 27, 2017 by uploading modified phase code data and a variable pulse repetition frequency (VPRF) table for both KuPR and KaPR at the National Aeronautics and Space Administration (NASA) Goddard Space Flight Center (GSFC). Fig. 4 shows a conceptual diagram of the DPR scan pattern during both normal and experimental observation. In the experiment, the KuPR scan pattern was changed to observe from nadir to about  $+34^\circ$ , similar to the TRMM end-of-mission experiment [14], [15]. The KaPR scan pattern was arranged to cover the scan angle of KuPR by KaMS and KaHS modes. The reason why wide swath observation is not performed symmetrically around nadir is that the observation gap opens when the number of angle bins in one scan is greater than 49 due to the fixed relationship between the satellite speed and DPR's scan speed. Assuming the radar's symmetric scan, analysis can even be conducted by only acquiring data on one side.

During the experiment, the DPR had successfully observed precipitation echo even at the large scan angle as well as at the normal scan angle. Fig. 5 depicts examples of the vertical cross sections of the received echo power by the KuPR and KaPR when obtaining precipitation echo around the Bay of Bengal. Scan No. 5767 of orbit No. 20308 on September 25, 2017 and scan No. 2479 of orbit No. 20332 on September 26, 2017 are chosen as the typical cases for normal observation [Fig. 5(a) and (c)] and wide swath observation [Fig. 5(b) and (d)], respectively. In the vertical cross section of the experiment shown in Fig. 5(b) and (d), the precipitation echoes are obtained at about 150 km distance from nadir not covered by the normal

observation. On the other hand, the precipitation echo near the surface becomes more difficult to discriminate as the scan angle becomes larger due to the severe contamination of surface echo in the beam direction (mainlobe clutter). Moreover, for KuPR in the experiment, unnatural received echo patterns appeared at the various scan angles. For example, the curves observed at around 100 km and 200 km are the fake echoes from sidelobe directions. The stripe patterns appeared at 225 km or more from nadir are also the fake echoes obtained from grating lobe direction. These are commonly recognized as the radar clutter problems of electrically steered planer antenna. The sidelobe and grating lobe clutters are not dominant in the KaPR data as shown in Fig. 5(d). Note that the gap at around 125 km in the KaPR experimental data in Fig. 5(d) is derived from the difference in the radar sensitivity between the KaMS and KaHS scans.

### III. ANALYSIS OF RADAR CLUTTER

#### A. Analysis Method

In order to statistically evaluate the occurrence frequency of radar clutter during the experiment, the clutter classification method shown in Fig. 6 was devised based on Kubota *et al.* [18]. The main difference between the method shown in Fig. 6 and that by Kubota *et al.* [18] is summarized in terms of the following two points.

The first point is the setting for the clutter-free bottom, the lowest range bin that is not affected by the mainlobe clutter. In the DPR L2 algorithm, the clutter-free bottom is calculated from the vertical profile of the received echo power and stored as "binClutterFreeBottom" in the L2 products. However, when the clutter-free bottom overlaps with a range bin affected by sidelobe/grating lobe clutter, the algorithm is designed to automatically select the next higher range bin as binClutterFreeBottom [19]. Consequently, mainlobe clutter height cannot be independently and accurately evaluated from binClutterFreeBottom. To construct an independent dataset of mainlobe clutter, based on the statistical occurrence of sidelobe clutter, the clutter-free bottom between angle bins 5 and 13, where the sidelobe effect overlaps the top of the mainlobe clutter, is defined by linear interpolation from the clutter-free bottom before and after. Similarly, in the region of angle bin No. 40 or more, where the influence of the grating lobe is large, the clutter-free bottom is linearly interpolated by using the characteristic of grating lobe clutter occurring at every other angle, as described in Section III-C.

The second point is the setting of a threshold for sidelobe/grating lobe clutter. Kubota *et al.* [18] utilized an approximated equation of the standard deviation of fading noise  $\sigma_N$  (Kumagai *et al.* [20]) as follows:

$$\sigma_N = \frac{\pi P_n}{\sqrt{6}} \sqrt{\frac{1}{N} + \frac{1}{M}}. \quad (1)$$

Here,  $P_n$  is the mean received power of the noise,  $N$  and  $M$  are the number of independent sample number of echo and noise, respectively. While the typical values of  $N = 102$  and  $M = 892$  were set for KuPR by Kubota *et al.* [18],  $N$  and  $M$  are set as the average values during the experiment for each Ku ( $N = 78$  and  $M = 604$ ), KaMS ( $N = 85$  and  $M = 526$ ), and KaHS ( $N = 75$  and  $M = 622$ ) observation in this study. By adopting

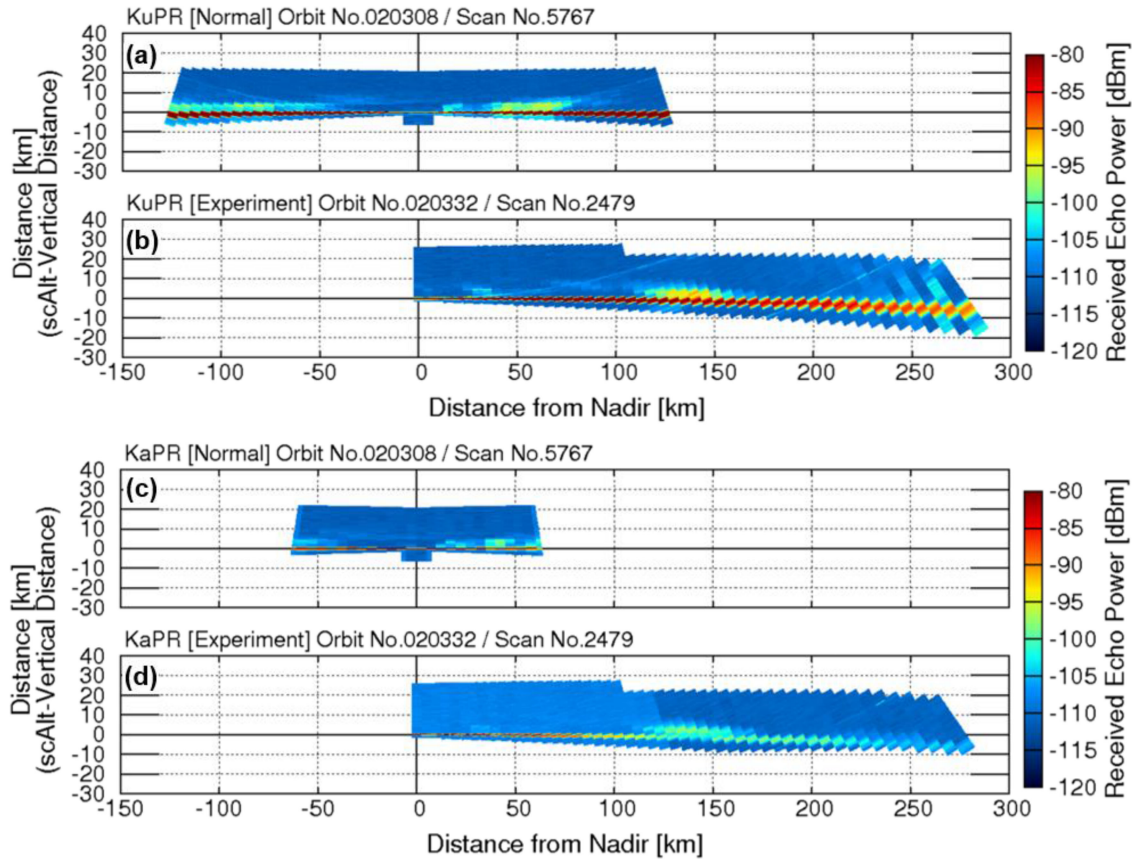


Fig. 5. Examples of vertical cross sections of received echo power in the real aspect ratio for (a) KuPR in normal observation and (b) in the experiment; (c) KaPR in normal observation and (d) in the experiment, respectively. The KaMS and KaHS scans are drawn in layers in (c).

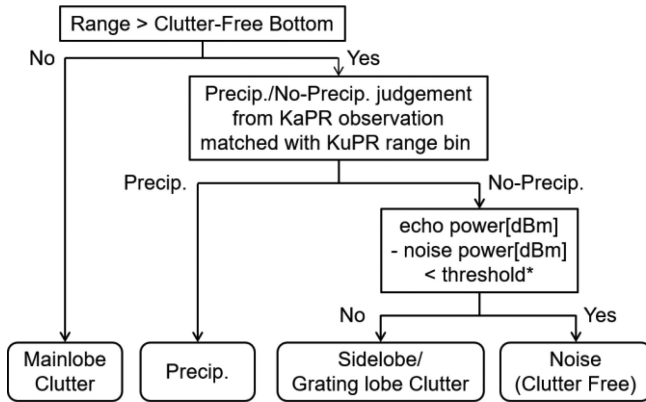


Fig. 6. Flowchart for diagnosing sidelobe/grating lobe clutter. The “threshold” for each observation mode is set as the value given in (3)–(5).

$3\sigma_N$  as the threshold of the clutter/nonclutter classification, the criteria set for each observation are given as

$$\begin{aligned}
 P_e &= P_s + P_n > P_n + 3\sigma_N = P_n + 3 \times \frac{\pi P_n}{\sqrt{6}} \sqrt{\frac{1}{N} + \frac{1}{M}} \\
 &> P_n \left( 1 + 3 \times \frac{\pi}{\sqrt{6}} \sqrt{\frac{1}{N} + \frac{1}{M}} \right) \quad (2)
 \end{aligned}$$

where  $P_e$  and  $P_s$  are the received power of echo and signal, respectively. Note that the actual values of  $N$  and  $M$  change dynamically since the DPR adopts the VPRF technique. In decibels, (2) can be converted to

$$P_{e,Ku} \text{ (dBm)} - P_{n,Ku} \text{ (dBm)} > 1.65 \quad (3)$$

$$P_{e,KaMS} \text{ (dBm)} - P_{n,KaMS} \text{ (dBm)} > 1.67 \quad (4)$$

$$P_{e,KaHS} \text{ (dBm)} - P_{n,KaHS} \text{ (dBm)} > 1.61. \quad (5)$$

These thresholds were actually used in Fig. 6 for clutter/nonclutter classification.

Fig. 7 summarizes the percentage of observations classified as mainlobe, sidelobe, and grating lobe clutters based on the flowchart in Fig. 6 relative to all observations during the experiment. Based on these results, the following sections investigate the occurrence mechanisms and characteristics of each type of clutter.

### B. Mainlobe Clutter

The clutter raid along the horizontal axis in Fig. 7 is mainlobe clutter that occurred due to surface echo contamination in the mainlobe direction. This clutter is often associated with spaceborne radar and reported as a main factor in the oversight of shallow storms [21], [22]. Because surface echo contamination becomes higher as the scan angle increases, the contaminated

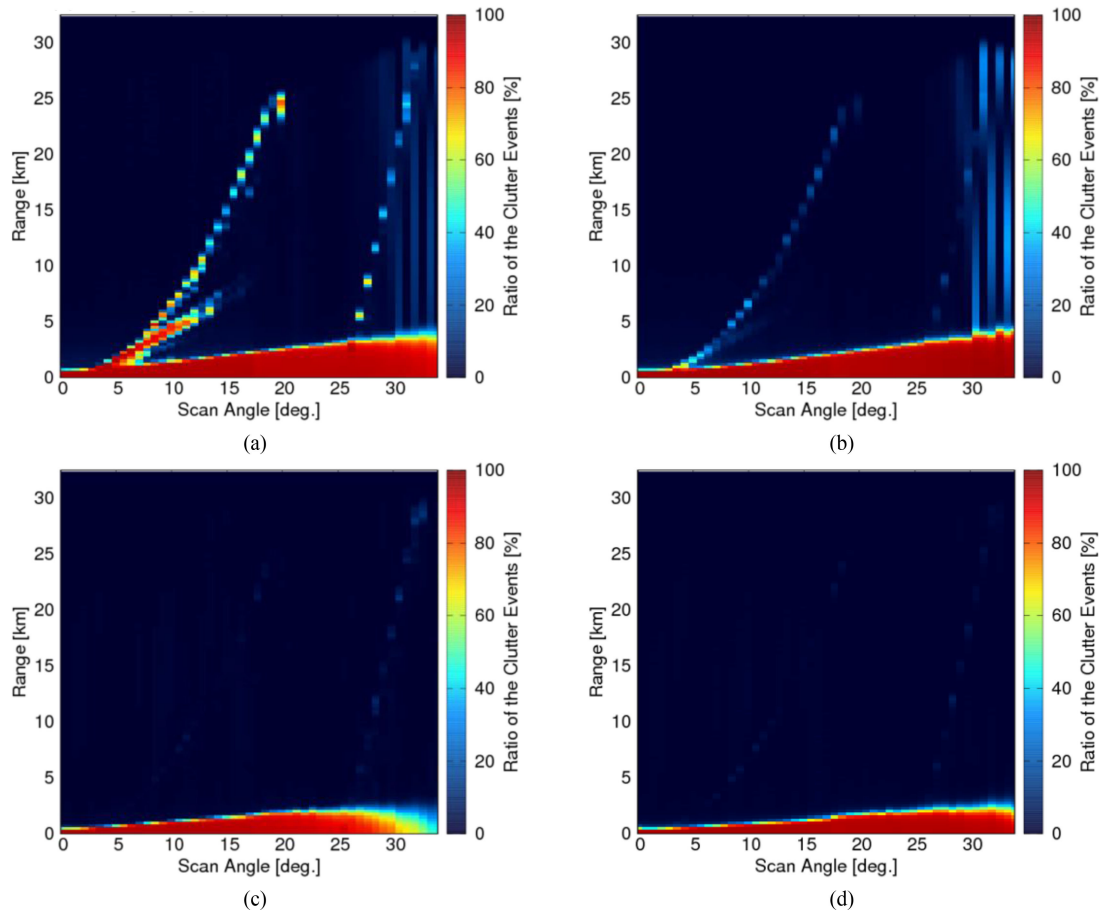


Fig. 7. Percentage of observations classified as clutter relative to all observations for (a) KuPR over ocean and (b) land; and (c) KaPR over ocean and (d) land during the experiment.

height (mainlobe clutter height) must be quantitatively assessed, especially in the wide swath observation.

As described in Section III-A, the original estimates of bin-ClutterFreeBottom entails uncertainty, particularly during this experiment; hence, the tentative clutter-free bottom used for the mainlobe clutter classification is also not fully reliable. For an independent and accurate assessment of the mainlobe clutter height, only scans that do not include the observed volumes classified as precipitation echoes and the sidelobe/grating lobe clutters in Fig. 6 are extracted and averaged to calculate the mean mainlobe clutter echo profiles. Then the mean height of the mainlobe clutter is calculated along the beam direction by setting the baseline thresholds as  $-110$ ,  $-108.5$ , and  $-110$  dBm, which are approximately 1 dB above the noise level for Ku, KaMS, and KaHS, respectively. For a comparison, the results when loosening the thresholds (with increments set to 1.0 dB for Ku and 0.5 dB for Ka) are derived as well. However, as seen in Fig. 5, the beam was actually tilted considerably near the maximum scan angle in this experiment, and the profile in the beam direction was no longer a vertical profile. Consequently, the mainlobe clutter height was estimated as the actual altitude considering the scan angle, which is equals to the vertical distance from the surface.

Fig. 8 summarizes the results of the estimated mainlobe clutter height in each scan angle. Fig. 8(a) and (b) indicate that the mainlobe clutter height of KuPR increases linearly along the incident angle both over land and ocean. However, over ocean, the increase in the mainlobe clutter height in a large scan angle is suppressed due to the decrease in the normalized radar cross section (NRCS) of at the surface ( $\sigma^0$ ) induced by strong quasi-specular scattering on the sea surface, as shown in Fig. 9. This tendency is more pronounced in the KaPR observation as the clutter height peaks at the scan angle of around  $26^\circ$  and then tends to decrease thereafter. This is due to the relatively low  $\sigma^0$  in KaPR brought by the lower transmitted power as compared to KuPR. Overall, the experiment showed that the mainlobe clutter could reach up to 1–4 km from the surface at large scan angles, which may mask precipitation echoes near the surface.

### C. Sidelobe Clutter

Clutter that increases its altitude as the scan angle increases below angle bin No. 30 in Fig. 7(a) and (b) is the typical sidelobe clutter observed by the TRMM's and GPM's radars as well [23]. A suppression method of these sidelobe clutters has already been developed and applied for the current DPR algorithm [18], [24].

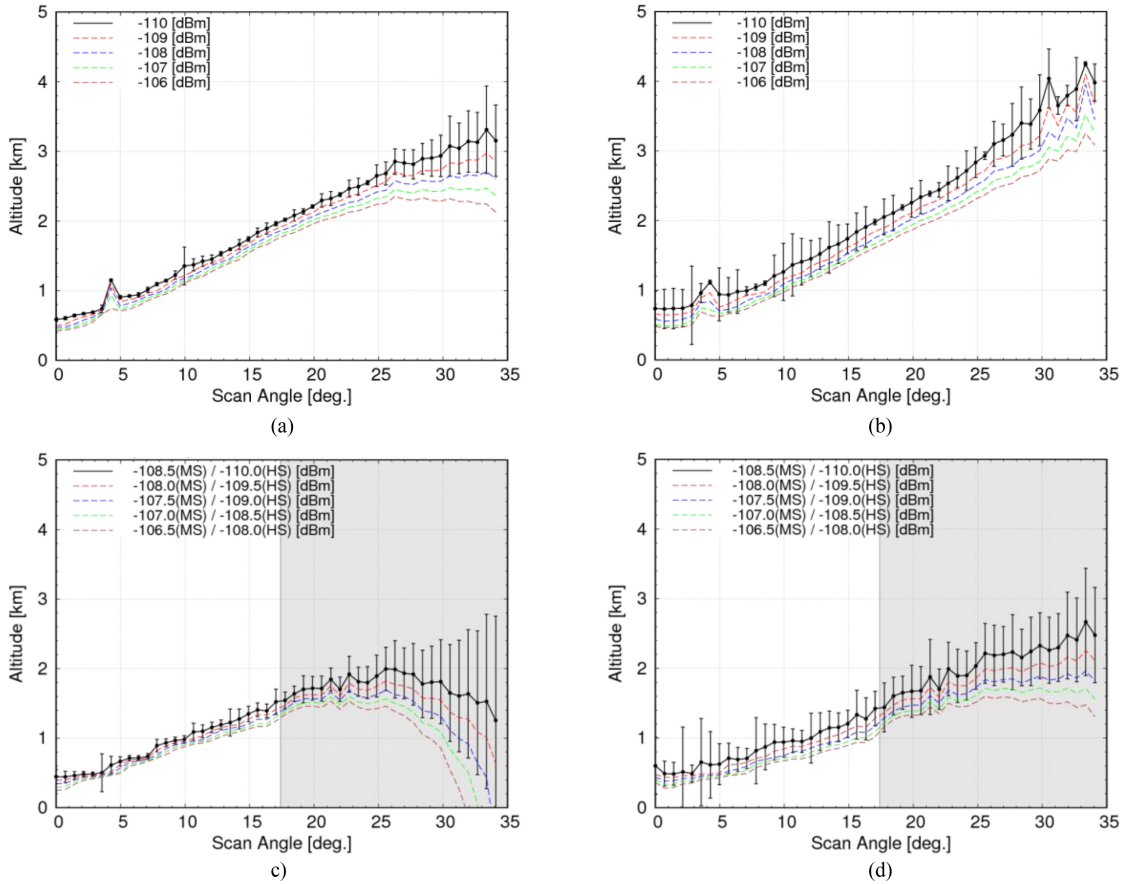


Fig. 8. Averaged mainlobe clutter height for (a) KuPR over ocean and (b) land; and (c) KaPR over ocean and (d) land during the experiment. The shaded area for (c) and (d) indicates the results from KaHS observation. The height is calculated as the actual altitude perpendicular to the ground surface. Bars indicate the standard deviation.

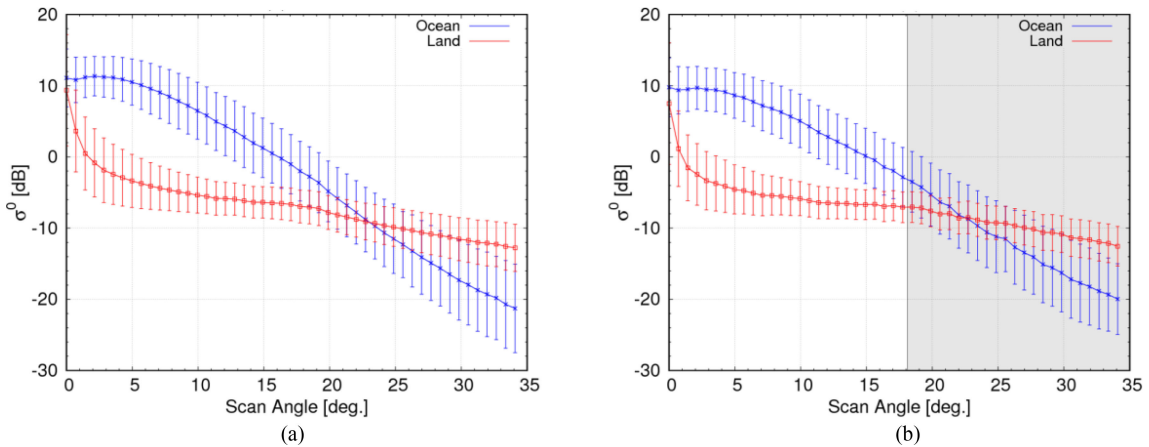


Fig. 9. Averaged  $\sigma^0$  for (a) KuPR and (b) KaPR during the experiment. The blue line is the result over ocean; the red line is the result over land. Bars indicate the standard deviation. The shaded area for (b) indicates the results from KaHS observation.

Furthermore, in this experiment, the sidelobe clutters at the large scan angles, which does not pose a risk of contamination in the normal observation mode, also appeared in Fig. 7(a) and (b) as a dotted line extending from angle bin No. 38 toward the sky. Sidelobe clutter occurs when the surface echo obtained from the sidelobe direction is strong enough compared to the echoes from the mainlobe direction, that is, mainly when the sidelobe

direction is directly below the satellite. Therefore, the frequency of sidelobe clutter occurrence tends to be high over the ocean surface where strong backscattering is obtained by the quasi-specular reflection and as mentioned in Section II-B, sidelobe clutter is also seen in KaPR, though very rarely [Fig. 7(c) and (d)]. Kubota *et al.* [24] showed that sidelobe clutter was more distinct in KaHS when the NRCS at the nadir was strong, while

intensities of sidelobe clutter in KaHS were much weaker than those in KuPR.

#### D. Grating Lobe Clutter

Grating lobes are the secondary maxima of directivity caused by the phase difference between each antenna element of the phased array antenna. Phase differences ( $\delta$ ) between each antenna element are defined as

$$\delta = \frac{2\pi}{\lambda} d (\sin\theta - \sin\theta_0) \quad (6)$$

where  $\lambda$  is the wavelength,  $d$  is the distance between each antenna element,  $\theta$  is the angle of the grating lobe direction, and  $\theta_0$  is the radar scan angle. To avoid grating lobe occurrence, this difference should satisfy the following:

$$|\delta| = \left| \frac{2\pi}{\lambda} d (\sin\theta - \sin\theta_0) \right| < 2\pi. \quad (7)$$

Considering  $-1 \leq \sin\theta \leq 1$ , the inequality can be interpreted as

$$|\delta| < \arcsin\left(\frac{\lambda}{d} - 1\right). \quad (8)$$

By substituting  $\lambda = 22.04$  mm,  $d = 16.6$  mm for KuPR, and  $\lambda = 8.43$  mm,  $d = 6.33$  mm for KaPR, the right side of (8) will be  $19.13^\circ$  for KuPR and  $19.38^\circ$  for KaPR, respectively. In normal observation, the DPR is designed to scan at  $\pm 17^\circ$ , which satisfies those inequalities. However, in this experiment, grating lobe contamination became prominent due to the large scan angle that exceeded the criteria of (8) and contributed to abnormally high received echo power. Similar to sidelobe clutter, grating lobe clutter is also prominent in KuPR [Fig. 7(a) and (b)] rather than in KaPR [Fig. 7(c) and (d)]. Note that grating lobe clutter was observed at every other angle bin because the timing of the receiving of the ground surface echo from the grating lobe direction moves across a plurality of receiving windows as the distance from the satellite to the ground surface in the grating lobe direction varies greatly depending on the scan angle. As a result, the grating lobe clutters appear alternately above and below the surface echoes from the mainlobe direction in this experiment.

Fig. 10 shows the case study used for grating lobe occurrence analysis. Here, grating lobe clutter occurrence at angle bin No. 48 (corresponding to a  $+33.37^\circ$  scan) is defined when the received echo power above the clutter-free bottom estimated in Section III-A exceeds a value which is 3 dBm larger than noise level under the no-rain condition, as illustrated in red along the satellite footprint with the daily sea ice data obtained by National Oceanic and Atmospheric Administration's (NOAA's) AUTOSNOW product [25]. The footprint of the grating lobe direction is also depicted as a black line in Fig. 10. In this case, the grating lobe direction is calculated at about  $-51^\circ$  using the following equation, transformed from (7)

$$\sin\theta = \pm \frac{\lambda}{d} + \sin\theta_0. \quad (9)$$

Looking at the relationship between the surface state of the grating lobe direction and grating lobe clutter occurrence, the fact that grating lobe clutter apparently occurred when the

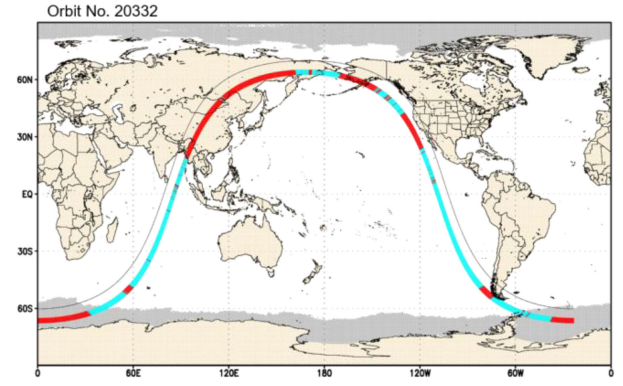


Fig. 10. Map showing the relationship between the surface state of the grating lobe direction and grating lobe clutter occurrence for the orbit No. 20332 in September 26, 2017. The thick light blue path is the scan footprint during the experiment; red shows grating lobe occurrence at a scan angle of  $+33.37^\circ$ . The black line is the footprint of the grating lobe direction ( $-51^\circ$ ) when the scan angle is  $+33.37^\circ$ . The gray shaded area is the sea ice region obtained by NOAA's AUTOSNOW product [26].

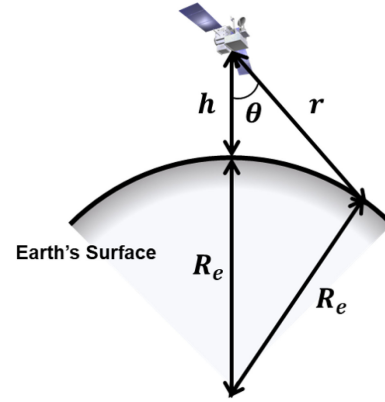


Fig. 11. Geometric relationship of a spherical earth approximation between the satellite, earth's surface, and grating lobe angle  $\theta$ .

ground surface of the grating lobe direction is land or sea ice can be easily found. During the experiment, about 92% of the grating lobe clutter in angle bin No. 48 occurred when the grating lobe directions were on land or sea ice. This is because relatively large backscattered surface echo can be obtained even from a slanted grating lobe angle when the surface is rough, as seen in the Fig. 9.

In Fig. 7(a) and (b), grating lobe clutter apparently started to occur in angle bin No. 40 (equals  $+27.69^\circ$ ), while grating lobes should emerge when the scan angle exceeds  $+19.13^\circ$  based on (8). The reason why no clutter occurred between those two scan angles can be partly considered in a simple geometric problem. If the grating lobe direction has no intersection with the earth's surface, there will be no backscattering and no grating lobe contamination. The distance from the satellite to the earth's surface ( $r$ ) when the grating direction touches the earth's surface can be calculated using the Pythagorean theorem below, assuming the simplified geometry shown in Fig. 11.

$$(h + R_e)^2 = r^2 + R_e^2. \quad (10)$$

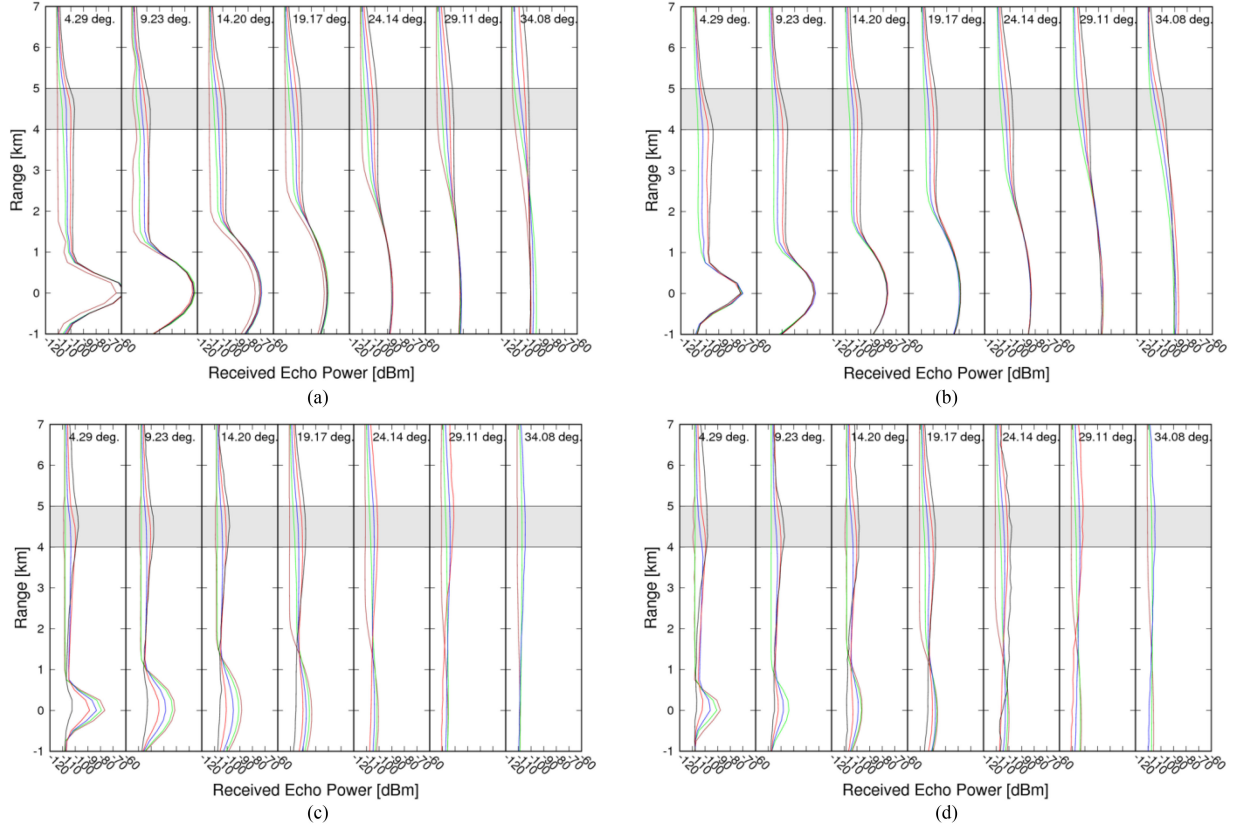


Fig. 12. Average echo profiles sorted by the mean echo power between 4 and 5 km from the surface for seven scan angles for (a) KuPR over ocean and (b) land; and (c) KaPR over ocean and (d) land during the experiment.

Here,  $R_e$  is the radius of the earth, and  $h$  is the mean satellite altitude. By substituting  $R_e = 6378.1$  km and  $h = 407$  km, we get  $r = 2314.6$  km. Because the relationship between the grating lobe angle and the radius of the earth can be written approximately using the law of cosines as

$$R_e^2 = (h + R_e)^2 + r^2 - 2r(h + R_e)^2 \cos\theta \quad (11)$$

the grating lobe direction ( $\theta_0$ ) tangent to the earth's surface is calculated as  $\theta = -70.5^\circ$ . Using (9), the angle which does not intersect the earth's surface is calculated to be  $+22.81^\circ$ . As a result, grating lobe clutter cannot occur at a scan angle of no more than  $+22.81^\circ$  [the closest scan angle that does not exceed this angle corresponds to  $+22.72^\circ$  (angle bin No. 33)], while grating lobes occur from  $+19.13^\circ$ .

For the scan angles between  $+22.81^\circ$  and  $+27.69^\circ$ , a relatively small NRCS and long propagation distance possibly contribute to less grating lobe contamination during the experiment. However, depending on the state of the earth's surface in the grating direction, it is undeniable that grating lobe clutter may occur even at these scan angles. The relationship between measured NCRS ( $\sigma_m^0$ ) and the received signal power at the surface ( $P_{r,s}$ ) is expressed by Kanemaru *et al.* [26] as

$$\sigma_m^0(\lambda, \theta_z) = \frac{2^9 \ln(2) \pi^2 \cos(\theta_z) r_s^2}{\lambda^2 G_r G_t L_p P_t \theta_{bp} \phi_b} P_{r,s}(r_s) \quad (12)$$

where  $\theta_z$  is the local zenith angle,  $r_s$  is the range from the radar to the earth's surface along the center of the radar beam,  $G_r$  is the

received antenna gain,  $G_t$  is the transmitted antenna gain,  $L_p$  is the peak loss power,  $P_t$  is the peak transmitted power,  $\theta_{bp}$  is the effective cross-track beam width, and  $\phi_b$  is the beam width in the along-track direction. Assume that the highest  $\sigma_m^0$  is about 0 dB (e.g., over dense forest area), the angle which brings the higher signal power than the noise level ( $-111$  dBm in this experiment) is approximately calculated as  $24^\circ$ . This result suggests that to limit the scan angle by  $\pm 23.43^\circ$ , roughly equivalent to a 355 km swath width with the orbit altitude of 407 km, is reasonable for KuPR. Note that the precipitation echo from the grating lobe direction is almost negligible since the surface echo is much stronger than the precipitation echo.

#### IV. CAPABILITY OF PRECIPITATION DETECTION

It has also been pointed out that if there is heavy precipitation, the strong echoes from heavy precipitation may overcome the echoes of the mainlobe clutter in Takahashi [15]. Therefore, the height of the mainlobe clutter obtained in Section III-B does not necessarily equal the altitude at which intense precipitation can be measured. To confirm this, the vertical profile of the received echo under the precipitation condition is shown in Fig. 12. At each scan angle ( $4.29^\circ$ ,  $9.23^\circ$ ,  $14.20^\circ$ ,  $19.17^\circ$ ,  $24.14^\circ$ ,  $29.11^\circ$ , and  $34.08^\circ$ ), averaged profiles are drawn for each mean echo power obtained at altitudes of 4–5 km. In each case, the mainlobe clutter height approximately equals the height from the ground to the inflection point of the profile and increases as the scan angle



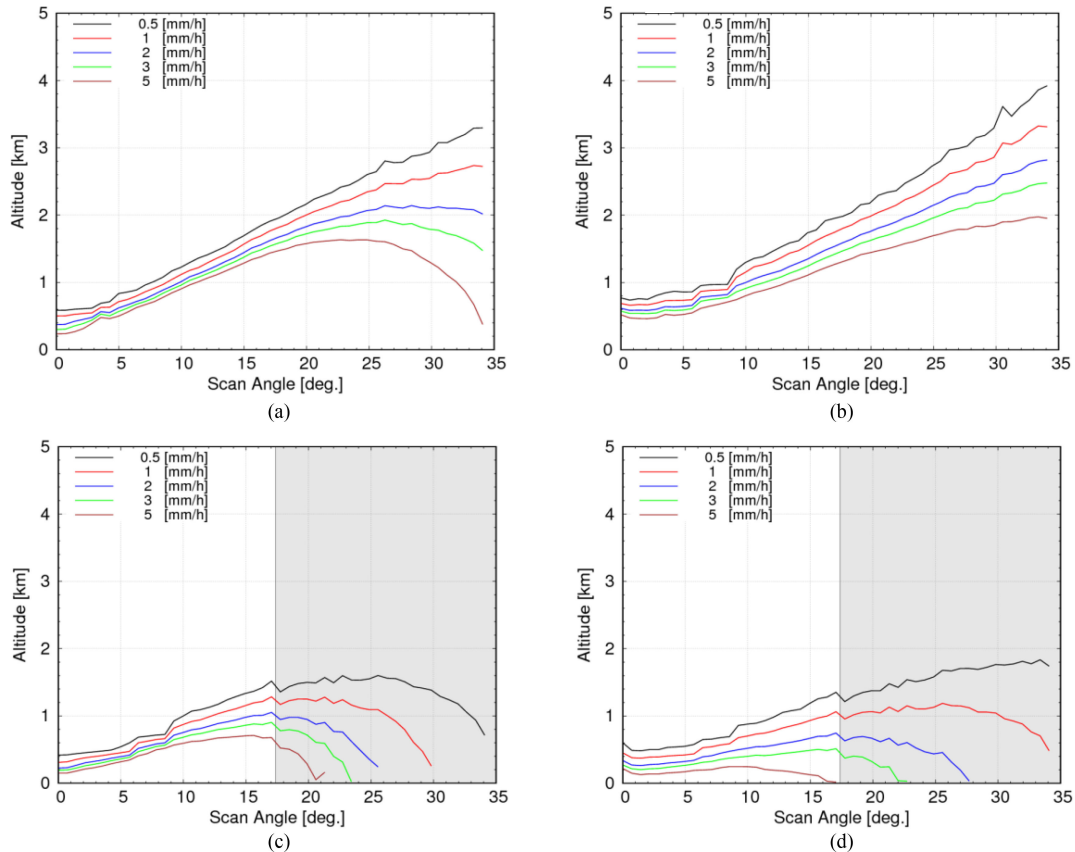


Fig. 13. Estimated observable height for each rainfall intensity for (a) KuPR over ocean and (b) land; and (c) KaPR over ocean and (d) land during the experiment. The shaded area for (c) and (d) indicates the results from KaHS observation.

increases as shown in Fig. 12. However, in the KuPR results shown in Fig. 12(a) and (b), the inflection point is relatively low in the profile when strong received echo was obtained at 4–5 km (i.e., the profile when heavy precipitation occurred). This suggests that mainlobe clutter is somehow masked during heavy precipitation, which may be observed below the height determined in the previous section. In the KaPR results shown in Fig. 12(c) and (d), this characteristic is hardly observable due to the large attenuation of precipitation, and the profile becomes almost flat at large scan angles.

In order to quantify how much precipitation can actually be observed at which altitude, we calculated how much precipitation intensity the mainlobe clutter would be if it were assumed to be equivalent to the precipitation signal. First, the profile of the measured radar reflectivity factor ( $Z$ ) under the no-rain condition was calculated from the received echo profile based on the radar equation, and then averaged for all observations during the experiment. Then, using the  $Z$ - $R$  power-law relation [27], observable heights for each precipitation intensity are estimated. Here, typical parameters for the rain are chosen ( $Z = 200R^{1.6}$ ). Finally, the estimated heights are converted to the actual altitude from the ground by considering the scan angle. Through this procedure, the observable heights for each precipitation intensity are estimated as shown in Fig. 13.

For all cases, the observable heights are lower in the case of heavy precipitation than in the case of light or no precipitation.

For instance, 5 mm/h precipitation can be seen from at least a 2 km altitude, while 0.5 mm/h precipitation may be masked up to 4 km in the worst case of the KuPR over land. Moreover, the observable height of intense precipitation tends to peak at a certain scan angle and then decrease at larger angles over ocean. Another point to note is that KaPR can observe precipitation of the same intensity in the lower altitude when compared to KuPR. KaPR can observe 0.5 mm/h precipitation at the altitude of at least no less than 2 km both over ocean and land. Especially over ocean, the decrease of the observable height at the large scan angles is prominent. Therefore, KaPR can be utilized to observe 5 mm/h precipitation at around 1.5 km altitude whereas KuPR cannot see them until about 3 km altitude, as seen in Fig. 13(a) and (c).

## V. SUMMARY AND DISCUSSION

The feasibility of wide swath observation for future spaceborne PR was evaluated using the data obtained by the wide swath observation experiment of the GPM DPR conducted on September 26 and 27, 2017. In the wide swath observation, the DPR measurements were contaminated not only by the mainlobe clutter reported by Takahashi [15] for the TRMM/PR, but also by the sidelobe and grating lobe clutters at the large scan angles. Those clutters observed during the experiment were classified based on the method shown in Fig. 6 and their characteristics and

occurrence mechanisms were discussed here. In addition, wide swath observations by the KaPR were regarded as new features in this study.

The mainlobe clutter height of KuPR increased linearly along the incident angle both over land and ocean, shown in Fig. 8(a) and (b). As shown in Fig. 13(a) and (b), 5 mm/h precipitation can be seen from at least a 2 km altitude, while 0.5 mm/h precipitation may be masked up to 4 km in the worst case of the KuPR. However, over ocean, the increase in the mainlobe clutter height in a large scan angle was suppressed due to the decrease in the  $\sigma^0$  on the sea surface, as shown in Fig. 9.

The major problem in wide swath observation with KuPR was the occurrence of grating lobe clutter. The grating lobe clutter apparently occurred when the ground surface of the grating lobe direction was land or sea ice. During the experiment, about 92% of the grating lobe clutter in angle bin No. 48 occurred when the grating lobe directions were on land or sea ice. This is because relatively large backscattered surface echo can be obtained even from a slanted grating lobe angle when the surface is rough, as seen in the Fig. 9.

There are two possible methods of reducing grating lobe clutter. The first method entails calculating the grating lobe echo by simulation based on the actual antenna pattern. Although this method is the most direct way of reducing the grating lobe in the algorithm, it is not realistic for the GPM DPR because the actual antenna pattern of the current DPR is hardly known due to the many changes in the phase code (that determines the antenna pattern) used by the phase shifters to mitigate the sidelobe interference [18]. This method may also be applicable to future KuPR provided that the antenna pattern is accurately obtained, while it requires a revision of the data processing algorithm. The second method is a statistical approach using the  $\sigma^0$  data of the grating lobe direction, similar to the method described by Kubota *et al.* [18]. This also should not be a candidate method because the grating lobe occurs in the direction approximately vertical to the scan angle [strictly saying, it changes as the scan angle changes based on the equation described in (9)] where there are no possibilities of the  $\sigma^0$  observation, even when assuming the  $\pm 34^\circ$  scan angle.

Therefore, the easiest way to avoid grating lobe contamination is to limit the scan angle within the angle where the grating lobe direction will not intersect with the earth's surface. As described in Section III-D, this angle corresponds to  $\pm 22.72^\circ$  for KuPR. However, there are almost no grating lobe clutters observed even at the scan angles no more than  $+27.69^\circ$  during the experiment. Thus, the maximum scan angle is calculated as the angle at which the received echo power does not exceed the noise level. By considering the largest NRCS from grating lobe direction, this angle is calculated as  $+23.43^\circ$ . At this scan angle, we can see the precipitation of intensity higher than 0.5 mm/h, at least from an altitude of 2.5 km [Fig. 13(a) and (b)].  $\pm 23.43^\circ$  electrical beam scanning approximately corresponds to 355 km swath width with the orbit altitude of 407 km.

For KaPR, the grating lobe contamination was not significant and precipitation at the lower altitude may have a chance to be detected, especially over the ocean, due to the lower mainlobe clutter height shown in Fig. 8(c) and (d). This was confirmed in

Fig. 13(c) and (d) showing the stronger precipitation signals can overcome the echoes of the mainlobe clutter at the lower altitude in the Ka. However, strong attenuation due to precipitation in the Ka-band may be an emerging problem. To retrieve the vertical profile of the precipitation rate,  $\sigma^0$  is utilized to estimate the path integrated attenuation (PIA) caused by the precipitation, and the attenuation in the precipitation profile is corrected using the PIA as the lower boundary condition via the surface reference technique (SRT) [17]. At a wide scan angle, however, the echo profile is flattened and results in large uncertainty in estimating  $\sigma^0$ . Due to this degradation, accurately estimating the precipitation profile at a large scan angle may be difficult. To determine the maximum scan angle of the KaPR quantitatively, further discussion on the reliability of PIA estimates is required. On top of that, a new algorithm instead of the SRT may be needed for precise precipitation estimation for future Ka-band radar that will observe at an even larger scan angle.

Furthermore, the fact that radar observes the slant profiles of the precipitation system, especially at a large scan angle, must be considered account in the precipitation retrievals. This also can be regarded as one of challenges in the future algorithm developments.

#### ACKNOWLEDGMENT

The authors wish to express their gratitude to the members of the GPM flight operation team at NASA GSFC for arranging this special observation experiment. The authors would like to thank the DPR Algorithm Development Team, under the NASA-JAXA Joint Algorithm Team.

#### REFERENCES

- [1] C. Kummerow, W. Barnes, T. Kozu, J. Shiue, and J. Simpson, "The tropical rainfall measuring mission (TRMM) sensor package," *J. Atmos. Oceanic Technol.*, vol. 15, no. 6, pp. 809–817, 1998.
- [2] T. Kozu *et al.*, "Development of precipitation radar onboard the tropical rainfall measuring mission satellite," *IEEE Geosci. Remote Sens.*, vol. 39, no. 1, pp. 102–116, Jan. 2001.
- [3] A. Y. Hou *et al.*, "The global precipitation measurement mission," *Bull. Amer. Meteorol. Soc.*, vol. 95, pp. 701–722, May 2014.
- [4] G. Skofronick-Jackson *et al.*, "The global precipitation measurement (GPM) mission for science and society," *Bull. Am. Meteorol. Soc.*, vol. 98, pp. 1679–1695, 2017.
- [5] M. Kojima *et al.*, "Dual-frequency precipitation radar (DPR) development on the global precipitation measurement (GPM) core observatory," in *Proc. Vol. 8528, Earth Observing Missions Sens.: Develop. Implementation Characterization II*, 85281A, Nov. 2012.
- [6] K. Furukawa *et al.*, "Satellite system test status of the dual-frequency precipitation radar on the global precipitation measurement core spacecraft," in *Proc. IEEE Int. Geosci. Remote Sens. Symp.*, 2013, pp. 1143–1146.
- [7] T. Kubota *et al.*, "Evaluation of precipitation estimates by at-launch codes of GPM/DPR algorithms using synthetic data from TRMM/PR observations," *IEEE J. Sel. Top. Appl. Earth Observ. Remote Sens.*, vol. 7, no. 9, pp. 3931–3944, Sep. 2014.
- [8] T. Iguchi, "Dual-frequency precipitation radar (DPR) on the global precipitation measurement (GPM) mission's core observatory," in *Satellite Precipitation Measurement*. Berlin, Germany: Springer, 2020.
- [9] C. D. Kummerow *et al.*, "The evolution of the goddard profiling algorithm to a fully parametric scheme," *J. Atmos. Oceanic Technol.*, vol. 32, pp. 2265–2280, 2015.
- [10] M. Greco *et al.*, "The GPM combined algorithm," *J. Atmos. Oceanic Technol.*, vol. 33, pp. 2225–2245, 2016.

- [11] C. Kidd, T. Matsui, J. Chern, K. Mohr, C. Kummerow, and D. Randel, "Global precipitation estimates from cross-track passive microwave observations using a physically based retrieval scheme," *J. Hydrometeorol.*, vol. 17, 2016, Art. no. 383550.
- [12] T. Kubota *et al.*, "Global satellite mapping of precipitation (GSMaP) products in the GPM era," in *Satellite Precipitation Measurement*. Berlin, Germany: Springer, 2020.
- [13] Y. Ikuta, "Data assimilation using GPM/DPR at JMA," in *WGNE Blue Book: Research Activities in Atmospheric and Ocean Modelling*, World Meteorological Organization, Geneva, Switzerland, No. 46, Section 1, 2016, pp. 11–12.
- [14] N. Takahashi *et al.*, "Overview of the end-of-mission observation experiments of precipitation radar onboard the tropical rainfall measuring mission satellite," *IEEE Trans. Geosci. Remote Sens.*, vol. 54, no. 6, pp. 3450–3459, Jun. 2016.
- [15] N. Takahashi, "Surface echo characteristics derived from the wide swath experiment of the precipitation radar onboard TRMM satellite during its end-of-mission operation," *IEEE Geosci. Remote Sens.*, vol. 55, no. 4, pp. 1988–1993, Apr. 2017.
- [16] S. Seto, and T. Iguchi, "Intercomparison of attenuation correction methods for the GPM dual-frequency precipitation radar," *J. Atmos. Oceanic Technol.*, vol. 32, pp. 915–926, May 2015.
- [17] R. Meneghini, H. Kim, L. Liao, J. A. Jones, and J. M. Kwiatkowski, "An initial assessment of the surface reference technique applied to data from the dual-frequency precipitation radar (DPR) on the GPM satellite," *J. Atmos. Ocean. Technol.*, vol. 32, no. 12, pp. 2281–2296, Dec. 2015.
- [18] T. Kubota *et al.*, "A statistical method for reducing sidelobe clutter for the Ku-band precipitation radar on board the GPM core observatory," *J. Atmos. Oceanic Technol.*, vol. 33, pp. 1413–1428, 2016.
- [19] T. Iguchi *et al.*, "GPM/DPR level-2 algorithm theoretical basis document (ATBD)," Oct. 2019. [Online]. Available: [https://www.eorc.jaxa.jp/GPM/doc/algorithm/ATBD\\_DPR\\_201708\\_whole\\_1.pdf](https://www.eorc.jaxa.jp/GPM/doc/algorithm/ATBD_DPR_201708_whole_1.pdf)
- [20] H. Kumagai, T. Kozu, and T. Iguchi, "Rain/no-rain discrimination for TRMM precipitation radar," in *Proc. IEEE Int. Geosci. Remote Sens. Symp. Remote Sens. – A Scientific Vision Sustain. Develop.*, 1997, pp. 1111–1113.
- [21] R. Marchand, G. G. Mace, T. Ackerman, and G. Stephens, "Hydrometeor detection using cloudsat—An earth-orbiting 94-GHz cloud radar," *J. Atmos. Oceanic Technol.*, vol. 25, pp. 519–533, 2008.
- [22] M. Hirose, S. Shimizu, R. Oki, T. Iguchi, D. A. Short, and K. Nakamura, "Incidence-angle dependency of TRMM PR rain estimates," *J. Atmos. Oceanic Technol.*, vol. 29, pp. 192–206, 2012.
- [23] H. Hanado and T. Ihara, "Evaluation of surface clutter for the design of the TRMM spaceborne radar," *IEEE Geosci. Remote Sens.*, vol. 30, no. 3, pp. 444–453, May 1992.
- [24] T. Kubota, T. Iguchi, T. Masaki, N. Yoshida and R. Oki, "Development of a statistical method for reducing sidelobe clutter in high sensitivity mode of GPM/KaPR," in *Proc. IEEE Int. Geosci. Remote Sens. Symp. Valencia*, 2018, pp. 8347–8348.
- [25] P. Romanov, G. Gutman, and I. Csizsar, "Automated monitoring of snow cover over North America with multispectral satellite data," *J. Appl. Meteor.*, vol. 39, no. 11, pp. 1866–1880, 2000.
- [26] K. Kanemaru, T. Iguchi, T. Masaki, and T. Kubota, "Estimates of spaceborne precipitation radar pulsewidth and beamwidth using sea surface echo data," *IEEE Trans. Geosci. Remote Sens.* to be published, 2020.
- [27] J. S. Marshall, R. C. Langille, and W. M. Palmer, "Measurement of rainfall by radar," *J. Meteor.*, vol. 4, pp. 186–192, 1947.
- [28] G. O. Young, "Synthetic structure of industrial plastics (Book style with paper title and editor)," in *Plastics*, vol. 3, J. Peters, Ed., 2nd ed. New York, NY, USA: McGraw-Hill, 1964, pp. 15–64.



**Kosuke Yamamoto** received the B.S. and M.S. degrees in engineering from Kyoto University, Kyoto, Japan, in 2015 and 2017, respectively.

Since 2017, he has been a Researcher with the Earth Observation Research Center, Japan Aerospace Exploration Agency, Tsukuba, Japan. His research interests include algorithm development for microwave remote sensing and its application to hydrological studies.

Kosuke Yamamoto is a Member of the Japan Society of Hydrology and Water Resources.



**Takuji Kubota** (Member, IEEE) received the B.S., M.S., and Ph.D. degrees in science from Kyoto University, Kyoto, Japan, in 1999, 2001, 2004, respectively.

From 2004 to 2005, he was a Postdoctoral Researcher with the Disaster Prevention Research Institute, Kyoto University. From 2005 to 2007 he was with Japanese Science Technology Agency. Since 2007, he has been a Researcher with the Earth Observation Research Center, Japan Aerospace Exploration Agency, Tsukuba, Japan. His research interests

include algorithm development for spaceborne radar and microwave radiometers for the TRMM, GPM, and EarthCARE missions.

Dr. Kubota is a Member of the Remote Sensing Society of Japan, Meteorological Society of Japan, Japan Geoscience Union, American Meteorological Society, and American Geophysical Union. He is the recipient of Prizes for Science and Technology in the Commendation for Science and Technology by the Minister of Education, Culture, Sports, Science and Technology, in 2016, and the Gambo-Tatehira Award by the Meteorological Society of Japan, in 2019.

**Nobuhiro Takahashi** received the B.S., M.S., and Ph.D. degrees in geophysics from Hokkaido University, Sapporo, Japan, in 1988, 1990, and 1994, respectively.

In 1994, he was with the National Institute of Information and Communications Technology (Communications Research Laboratory), Tokyo, Japan, where he was involved in the Tropical Rainfall Measuring Mission, the Global Precipitation Measurement Mission, and the Earth Clouds, Aerosols, and Radiation Explorer Mission. In 2015, he was with the Institute for Space-Earth Environmental Research, Nagoya University, Nagoya, Japan.

Dr. Takahashi is a Member of the American Meteorological Society and the Meteorological Society of Japan.



**Kaya Kanemaru** received the B.S. degree from Nagasaki University, Nagasaki, Japan, in 2009 and the M.S. and Ph.D. degrees from Nagoya University, Nagoya, Japan, in 2011 and 2014, respectively, all in science.

From 2014 to 2017, he was a Postdoctoral Researcher with the Earth Observation Research Center, Japan Aerospace Exploration Agency, Tsukuba, Japan. From 2017 to 2019, he was a Project Researcher with the Atmosphere and Ocean Research Institute, University of Tokyo, Kashiwa, Japan. Since

2019, he has been a Researcher with the Applied Electromagnetic Research Institute, National Institute of Information and Communications Technology, Koganei, Japan. His research interests include algorithm development and calibration for spaceborne microwave radar.

Dr. Kanemaru is a Member of the Meteorological Society of Japan.



**Takeshi Masaki** received the B.S. degree in science from Kochi University, Kochi, Japan, in 2006 and the M.S. degree in science from Kyoto University, Kyoto, Japan, in 2008.

Since 2009, he has been a Researcher with the Earth Environment Data Analysis and Research Group, Remote Sensing Technology Center of Japan, Tsukuba, Japan. His research interests include calibration and algorithm development for spaceborne microwave radar for the TRMM and GPM missions.



**Kinji Furukawa** received the B.S. degree in physics and the M.S. degree in geophysics from Tohoku University, Sendai, Japan, in 1988 and 1991, respectively.

In 1993, he was with the Japan Aerospace Exploration Agency (National Space Development Agency), Tokyo, Japan, where he was involved in the Tropical Rainfall Measuring Mission, the Global Precipitation Measurement Mission, and the Earth Clouds, Aerosols, and Radiation Explorer Mission.